Chapter 3

Impedimetric Immunosensor for the NS1 Dengue Biomarker Based on the Gold Nanorod Decorated Graphitic Carbon Nitride Modified Electrode

3.1 Introduction

Dengue is a nonspecific and self-limiting disease that has been one major global health concern in subtropical and tropical regions across the world [WHO 2012; Bhatt et al., 2013]. It has become the most important viral disease, with 50 to 100 million new cases every year. Dengue is a mosquito-borne disease mostly transmitted by infected Aedes aegypti spreading across 100 countries of the globe and categorized into four different serotypes (DENV 1-4) [Schaffner et al., 2014]. The disease has common undifferentiated symptoms, like fever which appear instantly after infection, and therefore it is necessary to anticipate a reliable diagnostic technique during the early stages of infection [Tang et al., 2012; Alcon et al., 2002]. Besides fever, nausea, vomiting, joint pain, and bleeding from the nose or gums are also symptoms of dengue. Detection of dengue through routine clinical care is quite challenging as the clinical and laboratory characteristics of dengue during the febrile phase, and the critical phase may overlap with other diseases rampant in the same endemic region. In primary infection, the level of NS1 varies from 0.04 to 2 μg/mL whereas, in secondary infection, it varies from 0.01 to 2 μg/mL. Cross-reactivity in flavivirus serology further compounded the diagnosis of dengue [Wang et al., 2020; Lapphra et al., 2008; Dussart et al., 2006; Guzman et al., 2016]. To reduce the morbidity and mortality rates of dengue infection, we need a faster diagnosis of dengue. NS1 is the non-structural protein that is dispensed into the bloodstream in quite a high concentration (up to μg/mL) and acts as a biomarker during the early hours of the infection [Alcon et al., 2002; Wang et al., 2020].

Conventional tests like ELISA bear limitation as it only allows antigen detection after five days of the onset of clinical symptoms [Guzman et al., 2010]. To facilitate a faster diagnosis, sensitive analytical tools should be developed which can detect a very low concentration of the antigen. Currently, various techniques are used for the diagnosis of Dengue disease, which comprise laboratory-based and point-of-care tests [Huang et al., 2013; Lim et al., 2018; Darwish et al., 2018]. Electrochemical biosensors provide an alternative to conventional techniques since they are highly sensitive, provide the desired selectivity, and even be transformed into portable devices [Peeling et al., 2010; Lee et al., 2017; Cecchetto et al., 2015; Palomar et al., 2018; Figueiredo et al., 2017; Junior et al., 2021; Arshad et al., 2020; Santos et al., 2020]. Unlike most colorimetric [Cecchetto et al., 2017] and fluorescence sensors [Wang et al., 2019], electrochemical sensors can assess analyte concentration and can also be used to indicate the status of viral infection in patients. Biosensors are characterized by receptors with high selectivity based on the biological sensing platform, for example, specific recognition of antigen to antibody and the detection of biological analytes in even complex media like blood serum. Electrochemical Impedance Spectroscopy (EIS) technique bears an advantage over other electrochemical techniques as they provide label-free detection of the analyte and its principle of sensing involves a variation of interfacial charge transfer resistance (R_{ct}) and capacitance of the biosensor electrode [Darwish et al., 2018; Orazem et al., 2008; Garrote et al., 2019, Xu et al., 2019; Bogomolova et al., 2009; Dijksma et al., 2002]. These corresponding variations can be correlated to analyte concentration immobilized at the surface of the biosensor and enable quantification of the analyte without any assistance of labels or markers. The sensitivity of the EIS biosensors is comparatively better, but it can be further improved by introducing nanomaterials. Numerous nanomaterials, such as AgNPs [Lazar et al.,

2016], AuNPs [Awan et al., 2020], MoS_2-Au [Deng et al., 2008], CNTs [Solanki et al., 2018], etc., have been reported to improve the EIS sensitivity in impedimetric measurement. The major problem in utilizing metal nanoparticles as the sensors is their low stability, and to overcome this problem, various materials such as SiO_2 [Bonanni et al., 2010], graphene oxide [Narayanan et al., 2003], reduced graphene oxide [Keller et al., 2010], carbon nanotubes [Zhang et al., 2010], and TiO_2 [Ensafi et al., 2015], etc. have been used as support. A wide range of literature is available in which graphene oxide and carbon nanotubes have been used as support. Still, as compared to them, very few reports are available in which graphitic carbon nitride (g-C_3N_4) has been used as support. g-C_3N_4 is a promising support material in catalysis. Its inimitable features such as easy synthesis procedure and functionalization, tunable bandgap, improved electronic properties, nontoxic and metal-free, good physicochemical stability, and environmentally friendly behavior are the advantages of g-C_3N_4 over carbon nanotubes and graphene oxide. As compared to carbon-based materials, which have been used as support, g-C_3N_4 is cost-effective because of its very easy synthesis, less time-consuming, and cheaper starting material required for synthesis. Due to these advantageous properties, g-C_3N_4 has been used for various applications such as electrochemical sensing, energy conversion and fuel cell, and electrochemiluminescence.

Graphitic carbon nitride (g-C_3N_4) is a metal-free semiconductor with an N-substituted graphitic π-conjugated layered structure. Additionally, the high N content of both pyridinic and graphitic N species makes the g-C_3N_4 a promising candidate for electrocatalytic reactions. The structure has repeated units of aromatic heptazine, which are connected through tertiary amines. g-C_3N_4 bears unique electronic, optical, and physiochemical properties, which present them as excellent 2D nanomaterials in the

field of photocatalytic degradation of pollutants [Li et al., 2020], bioimaging applications [Pang et al., 2009; Pham et al., 2021], optoelectronics [Liu et al., 2020]. However, the electrochemical behavior of g-C_3N_4 is poor due to poor conductivity and large contact resistance, which limit their application in the field of electrochemical sensing. The intrinsic structures of g-C_3N_4 have abundant coordinating sites for the metals capable of acting as catalytic active sites during the electrocatalytic process [Zhang et al., 2012].

In this chapter, first time, we are reporting an impedimetric immunosensor for Dengue biomarker NS1 based on an anti-NS1 modified g-C_3N_4 gold nanorod on GC electrode that is competent to sense and quantify NS1 at a clinically admissible concentration in phosphate buffer solution and also in the neat human serum sample. We have quantified Dengue virus 1 serotype using Anti-Dengue Virus 1+2+3+4 antibody. A long linear range (0.6 ng/mL to 216 ng/mL) with a detection limit of 0.09 ng/mL is obtained from the developed immunosensor.

3.2 Experimental

3.2.1 Chemicals and materials

Silver nitrate ($AgNO_3$), gold chloride ($AuHCl_4$), urea, glucose, L-Ascorbic acid, potassium ferrocyanide trihydrate $K_4[Fe(CN)_6].3H_2O$, potassium ferricyanide $K_3[Fe(CN)_6]$ and N-cetyl-N, N, N-Trimethyl ammonium bromide (CTAB) were bought from Sigma-Aldrich. Potassium dihydrogen phosphate KH_2PO_4 *dipotassium hydrogen orthophosphate* K_2HPO_4 has been used for the buffer preparation, NS1 antibody and antigen were purchased from Abcam with product code Anti-Dengue Virus 1+2+3+4 antibody (ab9202) Recombinant Dengue virus 1 NS1 protein (ab181950) and used without further purification. Blood serum (Human male) was procured from Prof D. Das lab, Institute of Medical Sciences (IMS), BHU, Varanasi ensuing the standard

procedure in agreement to respective guidelines. The experimental procedures were approved by the Biochemistry lab of the IMS, BHU, and as per the Institutional Ethical Committee and oral permission was gained from all subjects.

3.2.2 Instrumentation and characterization tools

Autolab (PGSTAT,302, The Netherlands) Potentiostat/Galvanostat was used for the electrochemical measurements (cyclic voltammetry and electrochemical impedance studies) in a three-electrode electrochemical setup using glassy carbon (GC) (CH Instruments, area = 0.07 cm^2) or modified GC as working electrode, platinum wire as counter electrode and Ag/AgCl (saturated with KCl) as a reference electrode. All the electrochemical measurements were performed at room temperature (25 ºC). Before electrochemical measurements, solutions were purged with high purity N_2 for 20-25 minutes. Before modification, GC electrode surface were polished mechanically on a wet polishing cloth using 0.05 µm size neutral alumina powder, rinsed thoroughly with triply distilled water, and then sonicated in an ultrasonic cleaning bath for 10 min. Finally, the electrodes were again rinsed with triply distilled water and allowed to dry at room temperature after ultrasonication. EPOCH2 microplate reader (Biotek) spectrophotometer was used to measure the spectra in the UV-visible region. The surface morphology was analyzed by using a scanning electron microscope [FE-SEM (Zeiss, Merlin)] working with accelerating voltage of 20 V to 30 kV, and the structural morphology of the samples was analyzed by using a transmission electron microscope (TEM) [FEI Tecnai-G2]. Rigaku miniflex 600 X-ray diffractometer with Ni-filtered Cu Kα radiation (λ = 1.54056 Å) was used to get the XRD pattern of the samples at a scan rate of 3º min^{-1}. The chemical composition of the material was investigated by a Thermoscientific K-Alpha X-ray photoelectron spectrometer (XPS).

3.2.3 Synthesis of g-C_3N_4

The thermal polymerization method is used to get g-C_3N_4 using urea precursor [Lin et al., 2014; Li et al., 2019]. In brief, 1g urea was first taken in an alumina crucible wrapped with aluminium foil and was heated directly in a muffle furnace at 550 ° C for four h with 3 °C/min heating rate. After that, it was naturally cooled down to room temperature and washed with water and ethanol several times, followed by drying at 80 °C in a vacuum oven.

3.2.4 Synthesis of AuNRs

AuNRs have been synthesized using the seed-mediated growth method [Zhou et al., 2018]. In the experiment, 5 mL of CTAB (200 mM) and 5 mL of $HAuCl_4$ (0.5 mM) solution were mixed with continuous stirring at 1000 rpm in a 50 mL stoppered conical flask. Further, 600 µL of $NaBH_4$ (10 mM) was added in a single slot to the above reaction mixture resulting in a yellowish-brown color seed solution. In addition, the growth solution was made separately by mixing 5 mL of $HAuCl_4$ (1 mM) and $AgNO_3$ (4 mM) to CTAB solution (200 mM, 25 mL) and ascorbic acid (100 mM, 0.275mL) to persuade the growth of AuNRs. Finally, 60 µL of seed solution prepared above was added with stirring into 50 mL of the growth solution. The stirring was stopped, and the reaction mixture was kept at 30 °C for 24 hours undisturbed for the full-length growth of the AuNRs. Finally, the uniform mixture of AuNRs has been prepared to have less CTAB by centrifuging at 12,000 rpm for 10 minutes and stored in a dark room at 30 °C.

3.2.5 Synthesis AuNRs-g-C_3N_4 composite

The sheets were exfoliated by dispersing 50 mg of g-C_3N_4 in water-ethanol mixed solvent (3:1) followed by ultrasonication for 14 hours. The exfoliated sheets were centrifuged at 8000 rpm and washed 3 times with water and ethanol. 10 mg of exfoliated sheets were added to 5 ml double distilled water and sonicated for 1 hour,

followed by the addition of 5 ml of synthesized gold nanorod (1mM) and again sonicated for 2 hours. The resultant composite was centrifuged at 8000 rpm for 10 mins and washed with water and ethanol. By varying the concentration of AuNRs (1mM, 0.75mM, 0.5mM, 0.25mM), four different composites were synthesized as 1:4, 1:3, 1:2, 1:1 respectively. The systematic pathways for the synthesis of AuNRs-g-C_3N_4 are shown in Figure 3.1.

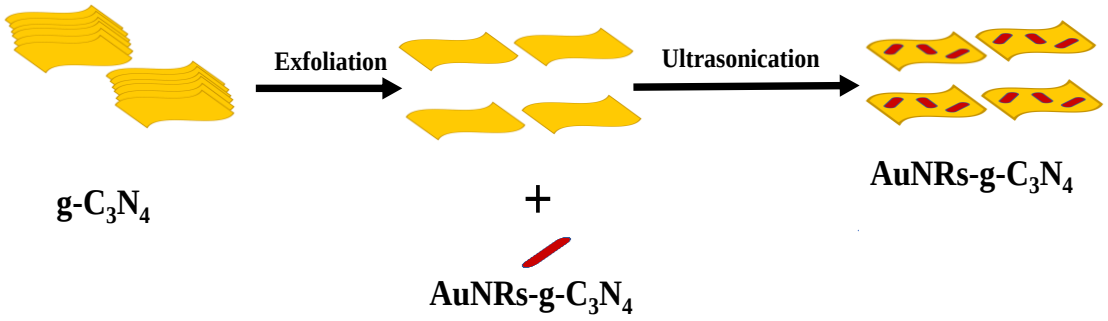

Figure 3.1 Schematics pathway for the synthesis of AuNRs modified graphitic carbon nitride.

3.2.6 Electrode Modification Procedure

The AuNRs and g-C_3N_4 modified GC electrode were prepared by drops casting the 10 µL of AuNRs (1.0 mM) and g-C_3N_4 solution (1mg/mL dispersion in water and ethanol of ratio 1:1 and Nafion binder) respectively onto the GC electrode surface and allowing to dry the at room temperature. The electrode was modified with AuNRs-g-C_3N_4 by drop-casting its 10 µL (1mg/mL dispersion in water and ethanol of ratio 1:1 and Nafion binder). For the immobilization of the anti-NS1, AuNRs-g-C_3N_4 modified electrode was washed with PBS buffer (pH= 7.4), and 10 µL of anti-NS1 (10µg/mL) was drop cast. The electrode was kept in moist condition overnight at room temperature for the immobilization of the antibody. Generally, dative binding, which is a physical interaction, may occur between antibody and AuNRs surface. It forms a covalent bond between the AuNRs and free sulfhydryl groups of the antibody [Fang et al., 2016]. After

incubation, the electrode was washed three times with a PBS buffer of pH 7.4 to eliminate unbound antibodies. Finally, the non-specific sites were blocked by immersing the electrode into 1% BSA in PBS buffer for 1 hour. The electrode was additionally washed three times with PBS buffer before their application in electrochemical measurement. During the EIS measurement, different concentrations of NS1 were spiked in the electrolyte 0.1M PBS buffer having 5mM of $[Fe(CN)_6]^{3-/4-}$. After each addition of the NS1, the electrode was incubated for 30 mins for its binding, and then EIS measurement was performed. The different NS1 concentration detected include 0.6, 1.6, 3.6, 11.5, 25.3, 70.6, 163.9, and 216 ng/mL. For the measurement in human serum, all steps are similar, except serum was used to block the nonspecific sites instead of BSA. Schematic presentation for electrode modification and dengue virus NS1 detection is given in Figure 3.2.

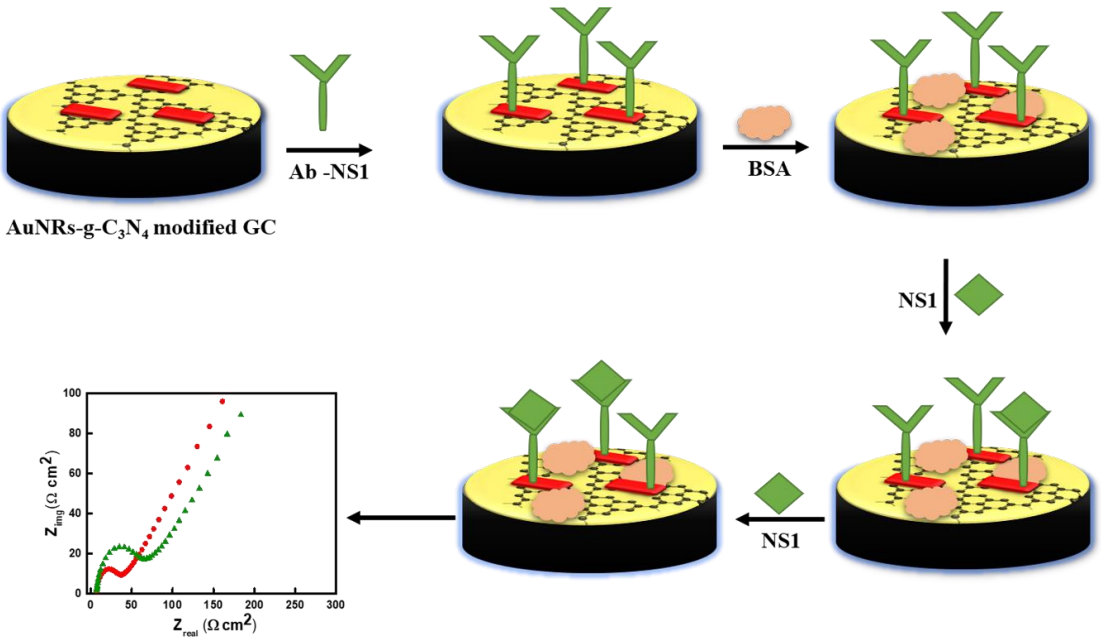

Figure 3.2 Schematic for the stepwise electrode surface modification and dengue virus NS1 detection.

3.3 Results and discussion

3.3.1 Characterization by UV-Visible and FTIR spectroscopy

The optical characteristics of the synthesized g-C_3N_4, AuNRs, and hybrid AuNRs-g-C_3N_4 nanocomposites were studied by UV-Vis spectroscopy. Figure 3.3(a) shows the representative UV-vis absorption spectra of all materials synthesized. The characteristic absorption peaks of g-C_3N_4 were observed at 328 and 390 nm, which could be due to conjugated network $\pi \rightarrow \pi^*$ transition and $n \rightarrow \pi^*$ transitions from the nitrogen nonbonding orbital to the aromatic nonbonding orbital, respectively, which are in accordance with previously reported literature [Jaiswal et al., 2020; Nikoobakht et al., 2003]. For AuNRs two well-defined absorption peaks were observed at 776 and 510 nm which are associated with the longitudinal and transverse electronic oscillation of AuNRs respectively and the observed peaks are in good agreement with the previous reports [Zhou et al., 2018]. In the case of nanohybrid (AuNRs-g-C_3N_4), representative peaks of g-C_3N_4 as well as of AuNRs are present, which confirms the successful incorporation AuNRs within or onto g-C_3N_4 surface.

FTIR spectroscopy (Figure 3.3(b)) was used to study the nature of the interactions of g-C_3N_4 with AuNRs. As we know that the displacement, disappearance, or appearance of the new bands in the FTIR spectra may be the consequence of interactions between AuNRs and g-C_3N_4. In the case of g-C_3N_4, the peak observed at 1632 cm^{-1} could be assigned to C=N stretching, and the different peaks observed at 1243, 1313, 1405, and 1464 cm^{-1} could be due to C-N stretching [Jazayeri et al., 2016; Kumar et al., 2019]. In the case of AuNRs, only one peak at 1635 cm^{-1} is observed, which could be due to -OH bending vibration of water molecules [Kumar et al., 2019]. In the case of nanohybrid AuNRs-g-C_3N_4, almost all the peaks were found, which are

present in g-C_3N_4, but here two additional peaks at 1583 and 1640 cm^{-1} were found, which indicates the good interaction of AuNRs with g-C_3N_4.

Figure 3.3(c) shows the XRD pattern of g-C_3N_4, AuNRs, and AuNRs-g-C_3N_4 nanohybrids. In the case of g-C_3N_4, the reflection observed at 27.4° and 13° corresponds to (0 0 2) and (1 0 0) crystal planes that show the interplanar stacking of the conjugated aromatic system and in-plane packing of g-C_3N_4 sheets, respectively. These observed results are consistent with the standard JCPDS file (JCPDS 87-1526) [Dai et al., 2013]. In the case of AuNRs, four additional peaks were observed at 38.2, 44.4, 64.6, and 77.5°, which corresponds to 111, 200, 220, and 311 planes of Au, respectively. In contrast, the AuNRs-g-C_3N_4 nanohybrid contains all the XRD peaks of g-C_3N_4 as well as AuNRs, which introduce another evidence to support the incorporation of AuNRs within or onto the surface of g-C_3N_4 sheet.

Additionally, we have characterized the prepared AuNRs and AuNRs-g-C_3N_4 via cyclic voltammetry techniques [Fahimirad et al., 2017]. Figure 3.3(d) shows the CVs of bare GC, C_3N_4 modified GC, AuNRs modified GC, and AuNRs-g-C_3N_4 modified GC, respectively, in 0.5 M H_2SO_4. In the case of AuNRs, a well-defined redox peak was observed at 0.88 and 0.51 V, which could be due to oxidation (Au^0 to Au^{3+}) and reduction (Au^{3+} to Au^0) of AuNRs. In the case of composite material (AuNRs-g-C_3N_4,) the oxidation peak was shifted to a higher potential (0.94V), overall peak separation was also increased, and the reduction peak was shifted to a slightly lower potential of 0.4; these changes in potential could be assigned to the slightly reduced electron transfer kinetics of AuNRs in g-C_3N_4 sheets.

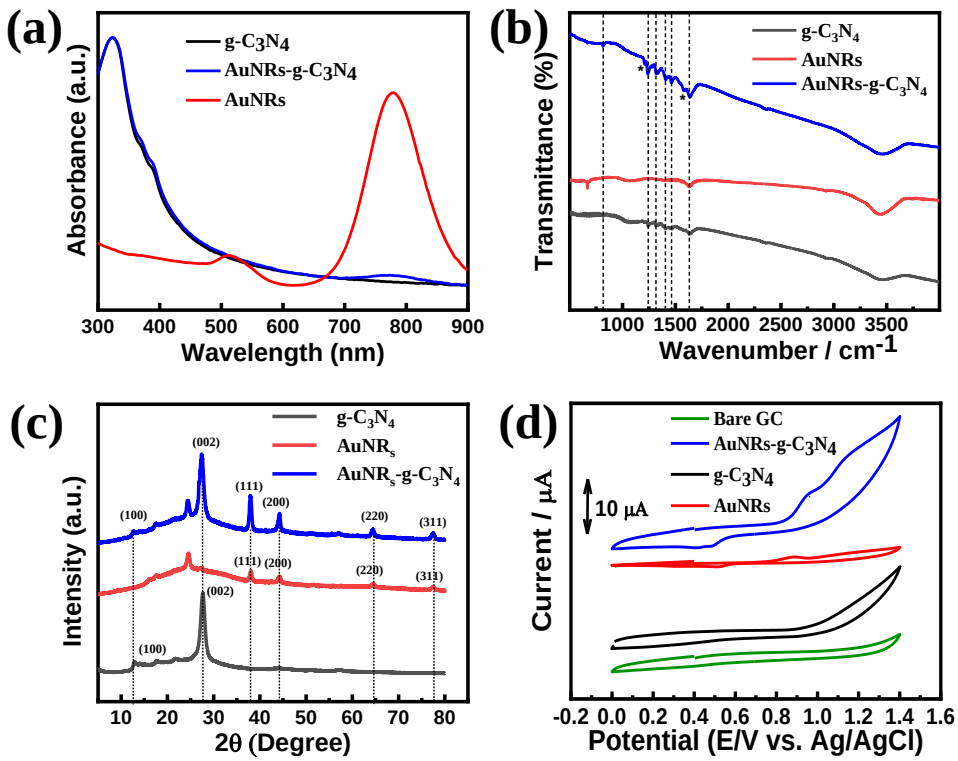

Figure 3.3 UV-visible (a), infrared (b), and powder XRD spectra of g-C_3N_4, AuNRs, and AuNRs-g-C_3N_4 (c), Cyclic voltammograms of bare GC, g-C_3N_4, AuNRs, and AuNRs-g-C_3N_4 in 0.5 M H_2SO_4 at a scan rate of 20 mVs^{-1}(d).

Figure 3.4(a) depicts the TEM images of g-C_3N_4 in which well-exfoliated sheets of g-C_3N_4 are easily visualized, which is very similar to the previous report [Truong et al., 2011]. Representative TEM images of AuNRs and AuNRs-g-C_3N_4 have been shown in Figure 3.4(b) and (c), respectively. Figure 3.4(d) shows the corresponding SAED pattern of Figure 3.4(c). Nice and uniform rod shape gold nanorods can clearly be seen in Figure 3.4(b). In composite material (AuNRs-g-C_3N_4), AuNRs were homogeneously distributed at the surface and also inside the g-C_3N_4 sheets (Figure 3.4(c)). The histogram represents the length and size distribution of the AuNRs. The average length of the AuNRs was found to be 32.5 nm (Figure 3.4 e), whereas the average diameter of AuNRs was found to be 14.5 nm (Figure 3.4f) For the detailed elemental composition of AuNRs-g-C_3N_4, Energy dispersive spectroscopy was done with elemental mapping

(refer to Figure 3.5). The result clearly suggests that the composition of carbon, nitrogen, and gold. In elemental mapping, distribution of AuNRs onto g-C_3N_4 is clearly visible.

3.3.2 TEM Characterization

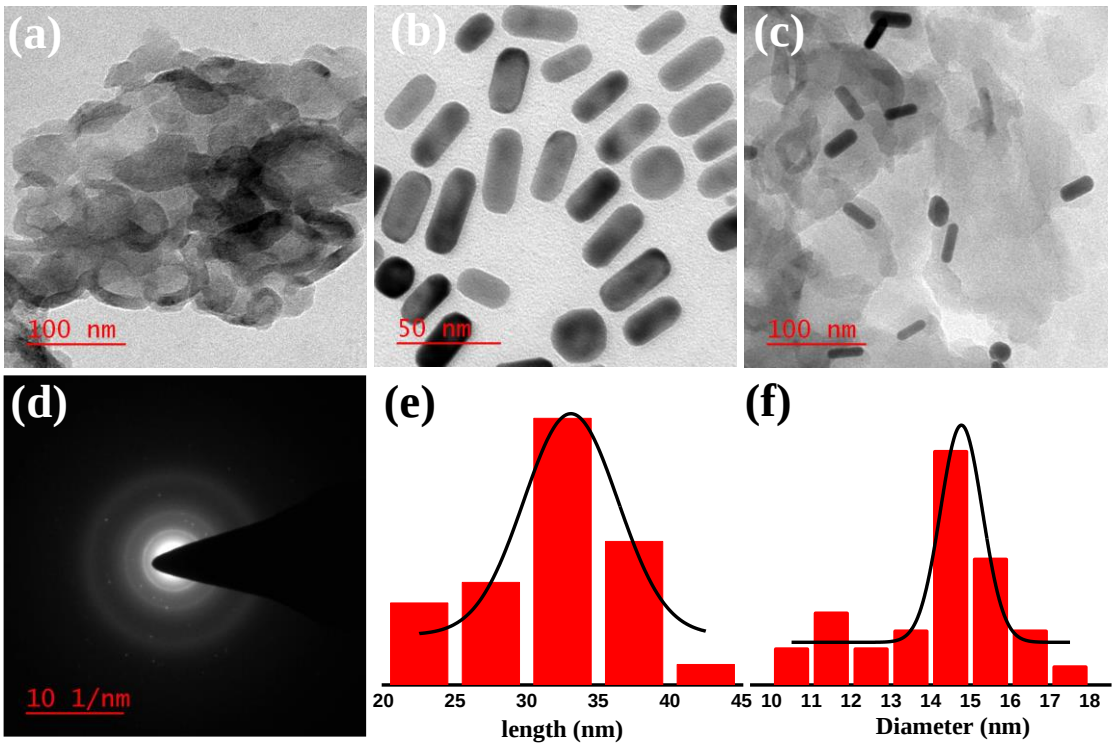

Figure 3.4 Shows the TEM images of graphitic carbon nitride (a), AuNRs (b), AuNRs-g-C_3N_4 (c), and SAED pattern of AuNRs-g-C_3N_4 (d). Histogram showing the average length (e) and diameter (f) of the AuNRs.

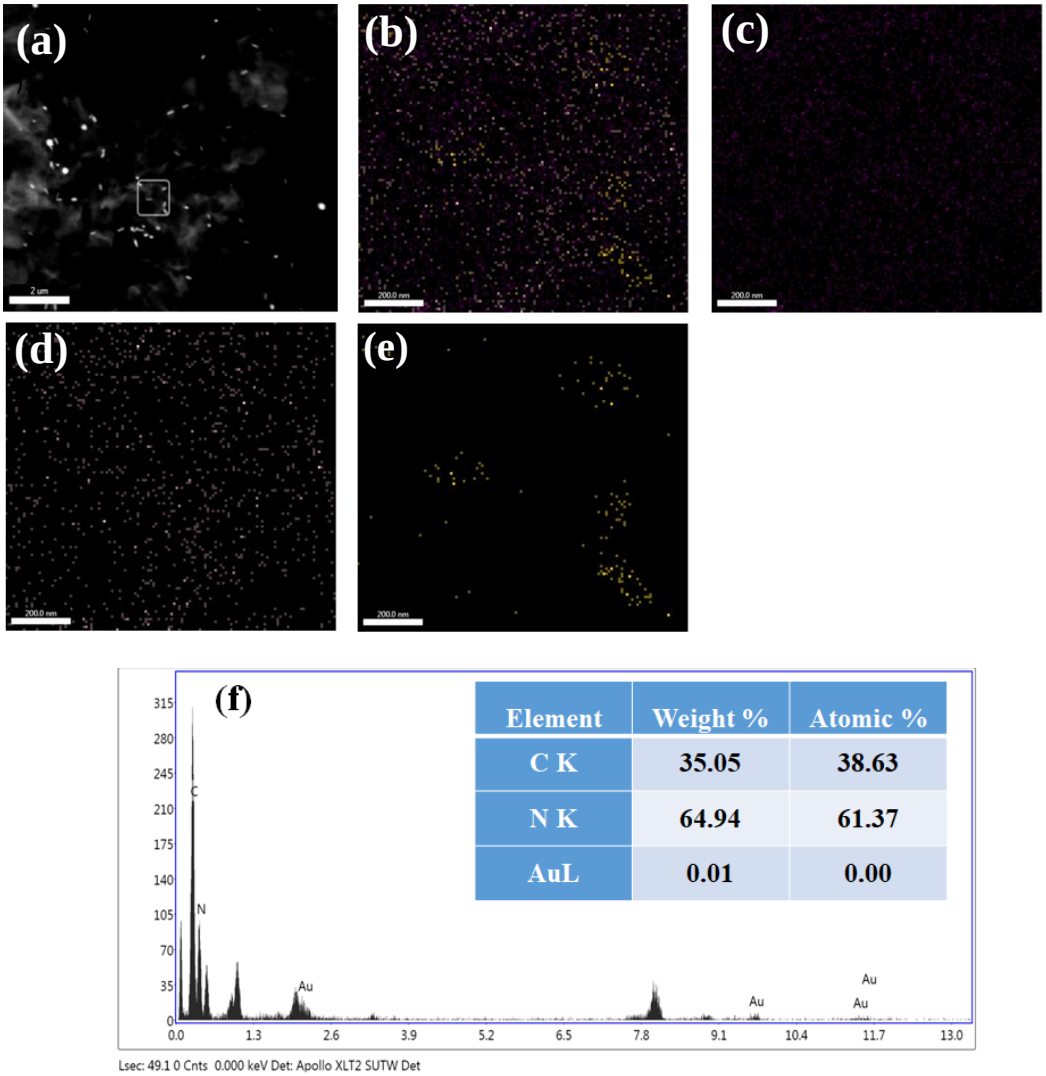

Figure 3.5. (a) DF-STEM images of AuNRs-g-C_3N_4 and (b) EDS Elemental mapping analysis of underlined area in (a) overlapped, (c) C, (d) N, (e) Au, and (f) EDS spectrum corresponding to underlined area with % composition.

3.3.3 Characterization by XPS

The detailed chemical composition of the sample has been investigated using XPS spectra. The detailed XPS survey spectra of all the synthesized materials g-C_3N_4, AuNRs, and g-C_3N_4-AuNRs are given in Figure 3.6(a). Three deconvoluted peaks at 284.78, 286.76, and 288.12 eV (as shown in Figure 3.6(b)) for C1s spectra in g-C_3N_4 and g-C_3N_4-AuNRs. The peak at 284.78 is due to pure graphitic sites present in the matrix (C-C) of carbon nitride, while peaks at 286.76 and 288.12 eV corresponds to sp^2

hybridized carbon (C-N-C) and sp^2 carbon attached to the NH_2 group (C-$(N)_3$) in the aromatic ring respectively [Ge et al., 2012].

Similarly, in Figure 3.6(c), the N 1s spectrum in g-C_3N_4 and AuNRs-g-C_3N_4 can also be deconvoluted into two peaks assigned at 398.77 and 400.62 eV, which are mainly for N-$(C)_3$ and N-H, respectively, inset shows the expended spectra of g-C_3N_4 from 396 to 400 eV. In the case of AuNRs-g-C_3N_4, one more peak was observed at 404.39 eV, which is due to π excitations [Elgrishi et al., 2018; Guo et al., 2019; Liu et al., 2011].

Further, Figure 3.6(d) shows the Au 4f spectra of AuNRs and AuNRs-g-C_3N_4. In AuNRs, the peaks corresponding to 83.67 and 87.35 eV in Au 4f spectra can be attributed to binding energies for Au $4f_{7/2}$ and Au $4f_{5/2}$, respectively, consistent with the values of Au^0 state [Miller et al., 2017]. In the case of AuNRs-g-C_3N_4, these peaks were slightly shifted to lower energy (83.34 and 86.99 eV) which confirms the binding of AuNRs with g-C_3N_4.

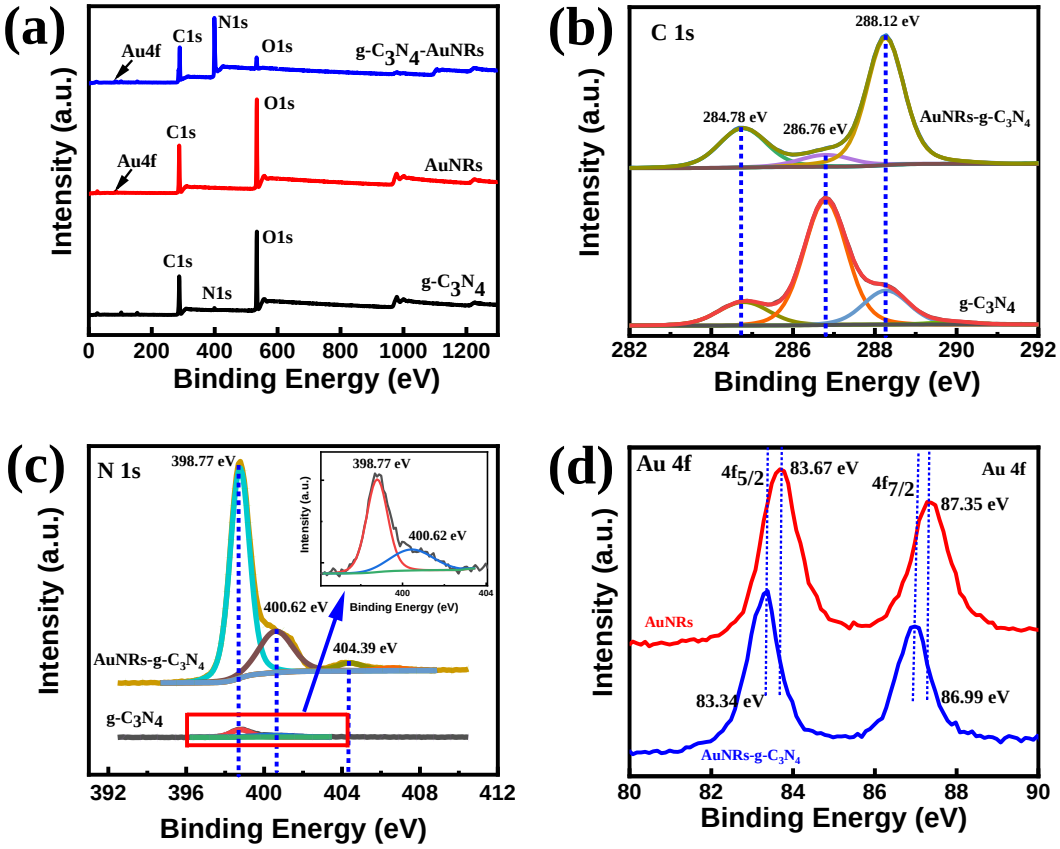

Figure 3.6 XPS survey spectra of g-C_3N_4, AuNRs and AuNRs-g-C_3N_4 (a), deconvoluted C 1s spectra of g-C_3N_4, and AuNRs-g-C_3N_4 (b), N 1s spectra of g-C_3N_4, and AuNRs-g-C_3N_4 (c) and Au 4f spectra of AuNRs and AuNRs-g-C_3N_4 (d).

3.3.4 Optimization of AuNRs and g-C_3N_4 Ratio

We have modified the electrodes with the inks, which were prepared by taking different weight ratios of AuNRs and g-C_3N_4. Cyclic voltammetry, as well as electrochemical impedance measurements, were recorded by taking $[Fe(CN)_6]^{3-/4-}$ as a redox couple (Figure 3.7). It was found that the 1:1 weight ratio shows the highest current and the least charge transfer resistance as compared to other weight ratios composition, so this weight ratio was used throughout the experiment. Further, the experimental Nyquist plots were fitted using the most appropriate equivalent circuit as shown in the inset of Figure 3.7 b.

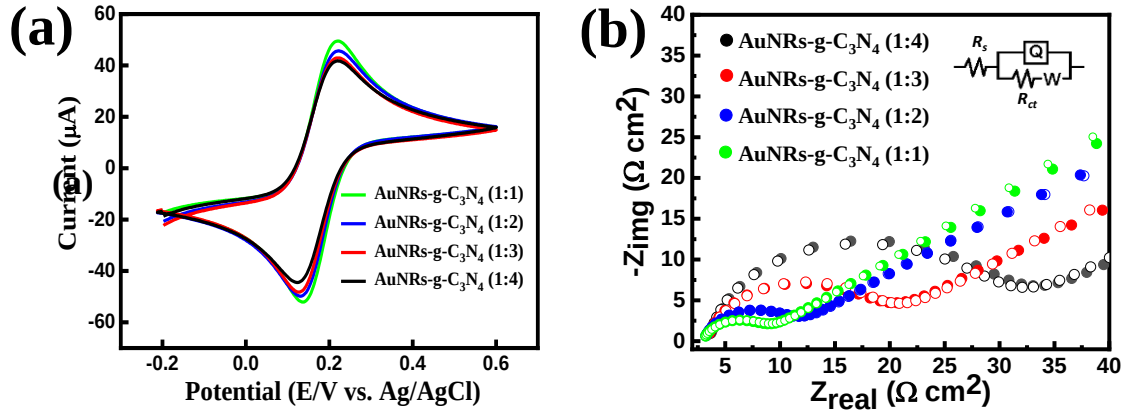

Figure 3.7. Cyclic voltammograms (a) and Nyquist plot (b) of AuNRs and g-C_3N_4 at different weight ratios. CVs and impedance spectra were recorded in 0.1M PBS (pH 7.4) having 5mM $[Fe(CN)_6]^{3-/4-}$.

3.3.5 Electrochemical characterization of the modified GCE.

At each and every step of biosensor probe preparation, the modified electrode was characterized by recording the cyclic voltammograms and electrochemical impedance in 0.1M PBS buffer (pH 7.4) and 5.0 mM $[Fe(CN)_6]^{3-/4-}$ as redox couple. Figure 3.8 (a) shows the cyclic voltammograms of GC, GC/g-C_3N_4, GC/AuNRs, and GC/AuNRs-g-C_3N_4. Here, if we compare the current and peak separation of GC/g-C_3N_4 and GC/AuNRs, then in the case of GC/AuNRs, peak separation was less in comparison to GC/g-C_3N_4. More importantly, in the case of GC/AuNRs, the current was also less as compared to GC/g-C_3N_4, which is mainly due to the low loading of AuNRs (more than 2.5 times less as compared to g-C_3N_4) of g-C_3N_4. Now, if we look at the final probe GC/AuNRs-g-C_3N_4, then, in this case, the current was surprisingly enhanced, which could be due to the synergetic effect of AuNRs with g-C_3N_4 sheets. Stepwise surface modification while biosensor construction was observed by CV and EIS measurement in the presence of 5.0 mM of $[Fe(CN)_6]^{3-/4-}$ in PBS (pH 7.4).

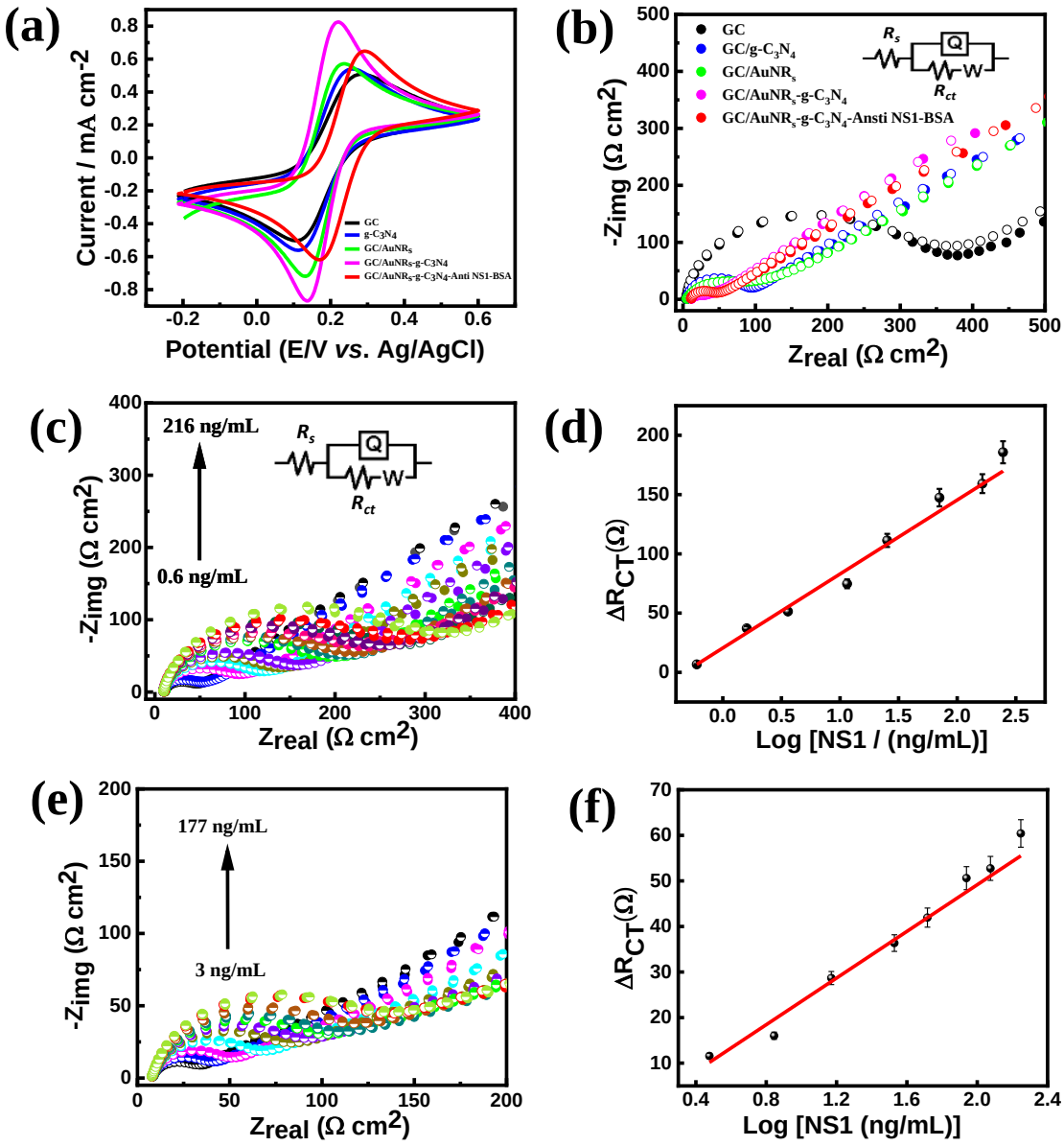

Figure 3.8 Cyclic voltammograms (a) and Nyquist plots (b) of GC, GC/g-C_3N_4, GC/AuNRs, GC/AuNRs-g-C_3N_4 and GC/AuNRs-g-C_3N_4/Anti NS1-BSA in PBS (pH 7.4). Nyquist plots for different concentrations of NS1 (0.6 to 216 ng mL^{-1}) at GC/AuNRs-g-C_3N_4/Anti NS1-BSA in PBS (c) and corresponding calibration plot (d). Nyquist plots in serum with various concentrations of NS1 (3 to 177 ng mL^{-1}) (e) and corresponding calibration plot (f) containing 5mM $[Fe(CN)_6]^{3-/4-}$. Inset of (c) shows the most compatible equivalent circuit. Filled circles represent the experimental result, whereas a blank circle represents the simulated result.

The CVs were performed in the potential window of -0.2 to 0.6 V (Figure 3.8(a)), and the EIS measurement was performed at 0.2 V (Figure 3.8(b)). From Figure

3.8(b), it can be inferenced that after the modification of the bare GC electrode surface with AuNRs-g-C_3N_4, the current was increased and charge transfer resistance was decreased, which confirms the successful immobilization/loading of AuNRs-g-C_3N_4 onto electrode surface due to which electron transfer kinetics was improved. After the modification of this probe with antibody significant decrease in current and enhancement in charge transfer resistance was observed, which confirms the successful immobilization antibody on AuNRs-g-C_3N_4 surface, and the decrease in current and increment in charge transfer-resistant is mainly due to the insulating nature of the antibody. Further, the Nyquist plot associated with each modification step was fitted with the most appropriate equivalent circuit (inset of Figure 3.8 b).

After the stepwise characterization of the sensor probe, we started to test the response of the sensor probe for the binding of dengue biomarker NS1 in PBS as well as in human serum sample, and the response was measured as a function of change in charge transfer resistance (R_{ct}) (Figure 3.8(c)). In PBS, upon binding of 0.6 ng/mL, charge transfer resistance was significantly increased, which confirms the binding of NS1 with Anti-NS1-BSA. The increment in R_{ct} is due to the shielding of the $AuNR_S$ surface, as a result of which accessibility of $[Fe(CN)_6]^{3-/4-}$ to the electrode surface and electron transfer process is reduced. For the estimation of analytical parameters such as sensitivity and limit of detection of the fabricated biomarker sensor, we have recorded the impedance with various concentrations of NS1 in PBS and human serum (Figure 3.8(c) and 3.8(e)). It was observed that with increasing the concentrations of biomarker NS1, the diameters of semicircles formed for the respective additions were increased. The immunosensor response was measured as a respective change in R_{ct} after binding with a particular NS1 concentration. Figure 3.8(c) and 3.8(e) show the Nyquist plots of immunosensor with various successive additions of NS1 in PBS and human serum. The R_{ct} values estimated

from the impedance spectra using the equivalent circuit (Inset of Figure 3.8(c)) were used to construct the calibration plot. The Nyquist plot associated with each additional step of NS1 in PBS as well as in human serum was fitted with the most appropriate equivalent circuit (inset of Figure 3.8b).

The change in charge transfer resistance (ΔR_{ct}) was plotted as a function of the concentration of NS1. The ΔR_{ct} was calculated by using the equation.

$$\mathbf{\Delta R_{ct} = R_{ct\ Final\ probe\ after\ binding\ with\ NS1} - R_{ct\ Final\ probe\ before\ binding\ with\ NS1}} \quad \text{(Eq 3.1)}$$

In PBS, the response of the prepared biosensor was found to be linear from 0.6 to 216 ng/mL (Figure 3.8(d)) with linear regression equation ΔR_{ct} = 20.5 + 62.4 log [NS1/(ng/mL)], R^2 = 0.99 whereas in human serum the response was found to be linear from 3 ng/mL to 177 ng/mL, R^2 = 0.98 (Figure 3.8f). For the construction of the calibration plot, three sets of experiments were performed, and show the standard deviation of the measurements (RSD = 2.9 - 4.5%) are shown by error bars, demonstrating good accuracy of the developed immunosensor. The limit of detection (LOD) for the constructed immunosensor was found to be 0.09 and 0.03 ng/mL in PBS and serum, respectively (LOD = $3S_b/m$, where S_b stands for the standard deviation of the blank signal and m stands for the slope of the linear portion of the calibration plot). The calculated LOD of the developed immunosensor was lower or comparable to the previously reported NS1 immunosensors as given in Table 3.1.

Table 3.1 Comparison table of the analytical parameters for the proposed NS1 immunosensor with previously reported sensors.

Transducer Surface	Method used for analysis	Limit of Detection (ng/mL)	Linear calibration range (ng/mL)	Reference
Modified gold electrode	Impedance	30	10 – 1000[a]	[Lee et al., 2017]
Modified gold electrode	Impedance	3	10 – 2000[b]	[Lee et al., 2017]
Au/Apramer/MCH	Impedance	0.05	0.01 – 1000[b]	[Figueiredo et al., 2017]
Au/Apramer/MCH	Impedance	0.02	0.01 – 100[a]	[Figueiredo et al., 2017]
MIP/PS-NF	Impedance	0.3	1 – 200[b]	[Junior et al., 2021]
Au/SAMs	Impedance	3	10 – 2000[b]	[Santos et al., 2020]
Au/SAMs	Impedance	30	10 – 1000[a]	[Santos et al., 2020]
Ag NPs	Impedance	0.5	3 – 300[b]	[Lazar et al., 2016]
MoS_2-Au	Impedance	1.67	40 – 2000[a]	[Deng et al., 2008]
Chitosan-carbon fiber	Amperometry	0.94	1 – 75[b]	[Guo et al., 2004]
SPCE-BSA	Impedance	0.3	1 – 200[b]	[Normand et al., 2001]
Functionalized SPGE	Impedance	0.5	1 – 25[b]	[Zhang et al., 2012]
PAH sandwiched CNTs	Impedance	35	100 – 2500[b]	[Cavalcanti et al., 2012]
AuNRs-g-C_3N_4	**Impedance**	**0.09**	**0.6– 216[b]**	**This work**

AuNRs-g-C_3N_4	**Impedance**	**0.03**	**3 – 177[a]**	**This work**

a = in serum, b = in PBS, CNTs = carbon nanotube, BSA = bovine serum albumin, SPCE = screen printed carbon electrode, MCH = 6-mercapto-1-hexanol, MIP = Molecularly imprinted polymer, PS-NF = polysulfone nanofiber, SPGE = screen-printed gold electrodes, SAMs = self-assembled monolayers.

Further, the cross-reactivity and selectivity of the developed immunosensor were checked with 1000 ng/mL of various other biologically related potentially interfering compounds like glucose, L-cysteine, and cholesterol. In Figure 3.9, the bar graph shows the response of the fabricated immunosensor with 1000 ng/mL of different biological interferences and 5 ng/mL of NS1. Different potentially related interfering compounds were studied in order to validate the sensor selectivity.

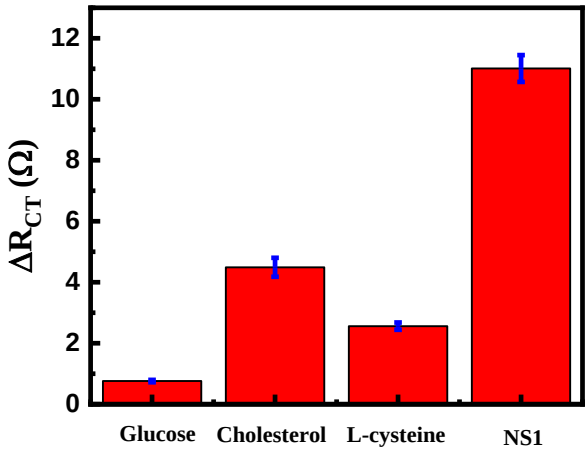

Figure 3.9 Interference study for the selectivity of NS1 immunosensor with various biological analytes. The interfering analytes concentration was 1000 ng/mL, and for NS1, it was 5 ng/mL

As shown in Figure 3.9, the immunosensor response was not significantly altered in presence of these biologically interfering compounds as compared to the high response in the presence of NS1, which confirms the better selectivity of the prepared immunosensor and its plausible application for the detection of NS1 without interference from related biological molecules and compounds.

For the real-time application of the developed immunosensor, we spiked the human blood serum (male), which was ten times diluted with 0.1 M PBS buffer of pH 7.4 with three known amounts (50, 100, and 120 ng) of NS1 and the percentage recovery was investigated using as developed immunosensor which has been shown in Table 3.2.

Table 3.2 Analytical recovery data for the proposed immunosensor spiked with a known amount of NS1 in human serum diluted ten times with 0.1 M PBS buffer of pH 7.4.

Amount of NS1 added (ng/mL)	Amount of NS1 found (ng/mL)	Relative Error %	Recovery %	Relative Standard Deviation (R.S.D.) %
50	48.5	3	97	3.2
100	104	4	104	2.3
120	116	3.3	96.6	4.1

The acceptable recoveries of NS1 were obtained with RSD varying from 2.3 to 4.1 % (n=3). These results confirm the acceptable accuracy of the proposed protocol, and the interferences have no significant effect on the immunosensor response signal hence the as-prepared immunosensor can be successfully applied for the quantification of NS1 in the presence of several other biomolecules. Further, to ratify the accuracy and sensitivity of the proposed immunosensor, we have compared the LOD and linear calibration range with the previously reported NS1 sensor (Table 3.1). From Table 3.1, it is clearly visible that the proposed sensor has a better LOD and linear calibration range. So, the developed immunosensor could be satisfactorily utilized for the accurate quantification of NS1 dengue biomarker.

As we know that reproducibility is one of the most significant aspects while limiting the commercialization of any developed biosensor. The reproducibility of the developed immunosensor was inspected by testing five different and freshly prepared electrodes

incubated with 10 µL of anti-NS1 (10 µg/mL, drop casted) antigen. Highly reproducible results were achieved with relative standard deviation (RSD = 2.5%) (Figure 3.10 a), signifying that the developed immunosensors shows more stable and reproducible result as compared to previously developed immunosensor [Nawaz et al., 2018; Sinawang et al., 2016]. Design and fabrication procedure could be the most probable reason behind the higher reproducibility of the fabricated NS1 immunosensor.

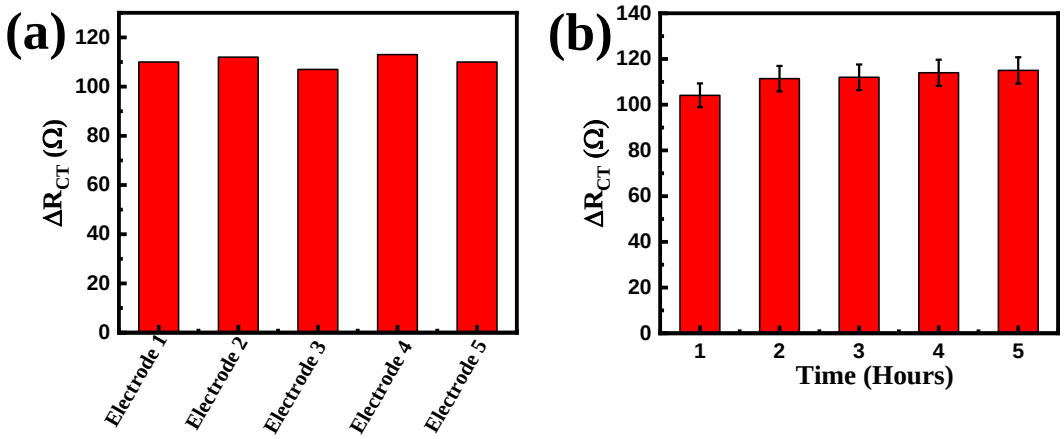

Figure 3.10. (a) The reproducibility study based change in charge transfer resistance of five different electrodes incubated with 10 µL of anti-NS1 (10 µg/mL, drop casted) antigen, (b) The stability study where the charge transfer resistance was measured with a different interval of time for the NS1 concentration of compared for electrodes tested with NS1concentration of 3.6 ng mL^{-1} for a period of 5 hours. The error bars indicate the standard deviation of three replicate measurements.

Further, we have also checked the operational stability of the constructed immunosensor by measuring the change in charge transfer resistance (R_{CT}) in PBS in the presence of NS1 (3.6 ng mL^{-1}) for 5 hours at an interval of one hour and very little alternation in response (R_{CT}) was observed (Figure 3.10 b), which confirms the better stability of developed immunosensor with lesser drift in signal over time.

3.4 Conclusion

In the present study, we have developed graphitic carbon nitride and gold nanorods based novel and label-free impedimetric immunosensor for dengue biomarker NS1, and its detection were done both in PBS and serum over a wide linear range. The constructed biosensor shows a linear response from 0.6 ng/mL to 216 ng/mL in PBS buffer, whereas in human serum, it shows a linear calibration range from 3 ng/mL to 177 ng/mL. The limit of detection was found to be 0.09 ng mL^{-1} and 0.03 ng mL^{-1} in PBS and human serum, respectively. The analytical parameters obtained by using this sensor were found to be superior and comparable to the earlier reported NS1 sensor. The present study indicates that the prepared immunosensor can act as a potential impedimetric technique for the point-of-care diagnosis of the dengue virus in biological samples.